AIAA JOURNAL
Vol. 39, No. 5, May 2001

Numerical Prediction of Interference Drag of Strut–Surface Intersection in Transonic Flow

Philippe-André Tétrault,* Joseph A. Schetz,† and Bernard Grossman‡
Virginia Polytechnic Institute and State University, Blacksburg, Virginia 24061

The numerical evaluation of the interference drag produced by a streamlined strut intersecting a flat wall in transonic flow is presented. The calculations were performed on unstructured grids using the FUN2D and FUN3D codes and the Spalart–Allmaras turbulence model (Spalart, P. R., and Allmaras, S. R.,"A One-Equation Turbulence Model for Aerodynamic Flows," AIAA Paper 92-0439, Jan. 1992). The grids were generated with AFLR2 and VGRIDns. The impact of the thickness-to-chord ratio of the strut, the Reynolds number, and the effect of the dihedral angle made by the strut with the wall are studied for both inviscid and viscous flows. To better understand the flow in the region where the strut and the wall intersect, the flowfield is analyzed in a detailed fashion for the thicker strut with pressure contours and stream traces. When the thickness-to-chord ratio of the strut is reduced, the flowfield is disturbed only locally at the intersection of the strut with the wall. The interference drag is calculated as the drag increment of the arrangement compared to an equivalent two-dimensional strut of the same cross section. The results show a rapid increase of the interference drag as the angle of the strut deviates from a position perpendicular to the wall. Separation regions appear for low intersection angles, but the viscosity generally provides a positive effect in alleviating the strength of the shock near the junction and, thus, the drag penalty. This study provides an equation to estimate the interference drag of simple intersections in transonic flow.

Nomenclature

c	=	chord
$C_{D_{\text{interf}}}$	=	interference drag coefficient; Eq. (9)
C_{D_p}	=	pressure drag coefficient
C_{D_S}	=	drag coefficient of the strut alone
$C_{D_{S+W}}$	=	drag coefficient of the strut–wall configuration
$C_{D_{\text{tot}}}$	=	total drag coefficient of a three-dimensional body
C_{D_v}	=	skin-friction drag coefficient
C_{L_S}	=	lift coefficient of the strut alone
$C_{L_{S+W}}$	=	lift coefficient of the strut–wall configuration
C_n	=	normal force coefficient
C_p	=	pressure coefficient
D_{interf}	=	interference drag; Eq. (8)
D_S	=	drag of the strut alone
D_{S+W}	=	drag of the strut–wall configuration
M_∞	=	freestream Mach number
Re_c	=	Reynolds number based on the chord
S_{ref}	=	reference area
t	=	thickness
x	=	distance measured from strut leading edge
y	=	spanwise distance from intersection
α	=	angle of attack
η	=	fraction of the span length
ϕ	=	strut–wall intersection angle; Fig. 1

Introduction

THE study of the interference drag produced in junctions is of considerable interest. In transonic flow, the interference between the components can produce unwanted shock waves and separated flow regions. It can have a detrimental effect on the total drag and, hence, the performance of the airplane if care is not taken in properly designing these intersections. In recent years, computational fluid dynamics (CFD) has been applied to the study of the interaction phenomenon involved at transonic speeds for such arrangements as wing–pylon,[1] wing–body,[2,3] and complete aircraft configurations.[4]

Multidisciplinary design optimization (MDO) studies conducted at Virginia Polytechnic Institute and State University[5,6] have focused on the design of a strut-braced wing transonic transport to carry 325 passengers at a cruise Mach number of 0.85. The overall design achieves a significant reduction of the drag and the takeoff gross weight. However, the aerodynamic interference drag at the wing–fuselage and wing–strut junctions is critical for the success of the design and needs to be evaluated accurately.

Several studies have been made of the flow around strut–endwall arrangements. In subsonic flow, Hoerner[7] used experimental data to determine the interference drag of various arrangements. The drag of a wing or strut intersecting a plane wall was studied. It was shown that the drag increases significantly as the pitch or lateral angles of the strut are varied from a position normal to the wall. Increases in the thickness-to-chord ratio of the strut cause a large increment in drag in the presence of a plane wall.

Kubendran et al.[8] conducted an experiment for the subsonic flow around a wing–fuselage juncture. The juncture was simulated by attaching a body of constant thickness with an elliptical leading-edge radius to a flat plate. They obtained favorable interference equivalent to −3% of the total drag of the plate and body in isolation. Barber[9] measured the intersection losses for a strut perpendicular to a wall in a low-speed wind tunnel. The struts studied had t/c ratios of 20 and 30%. Lower drag penalty was observed for thicker incident boundary layers than for thinner ones. In subsonic flow, Roach and Turner[10] tested a number of strut sections perpendicular to a wall. For streamlined strut sections of small aspect ratio, the secondary losses could be reduced to a correlation in terms of the Reynolds number of the flow, the Mach number, the thickness-to-chord ratio of the strut, and the displacement thickness of the incident boundary layer. Pierce and Nath[11] investigated the interference drag of a streamlined body with a thickness-to-chord ratio of 42.6%. The study showed a significant drag increase due to the junction. When compared to similar studies, the results confirmed the dependence of the interference drag on the thickness-to-chord ratio of the strut.

The objective of this paper is to provide a methodology to predict the interference drag produced by simple intersections in transonic flow. Analyses are performed by solving the Euler and Navier–Stokes equations on unstructured grids. The numerical tools are validated against experimental data for juncture flow, and the accuracy of the method is assessed. The case of a strut between parallel walls (see Fig. 1 for an example of strut between parallel walls in

Received 11 March 2000; revision received 3 October 2000; accepted for publication 9 October 2000.

*Graduate Student, Department of Aerospace and Ocean Engineering. Student Member AIAA.
†Fred D. Durham Chair, Department of Aerospace and Ocean Engineering. Fellow AIAA.
‡Department Head, Department of Aerospace and Ocean Engineering. Associate Fellow AIAA.

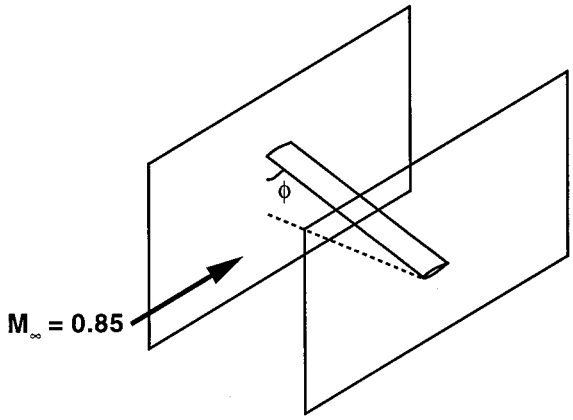

Fig. 1 Strut between parallel walls in transonic flow.

transonic flow) is analyzed for various angles and thicknesses of the strut. Cross sections in the near-wall flowfield are presented to explain the detailed behavior of the flow in the intersection region for the thickest strut section. The nondimensional interference drag results are represented by a response surface to aid in the use of these results for design studies. More details about the study at hand can be obtained from Tétrault.[12]

Modeling of the Problem

Flow Solver

The Euler and the Reynolds-averaged Navier–Stokes equations were solved for two-dimensional and three-dimensional problems with the codes FUN2D and FUN3D[13,14] from NASA Langley Research Center. The codes use an implicit, upwind, second-order accurate in space, finite volume discretization on unstructured grids, and the dependent variables are stored at the nodes of the cells. Roe's flux-difference splitting scheme[15] is used to compute the inviscid fluxes at the cell faces. The equations are integrated in time with the backward-Euler time-stepping scheme. For the two-dimensional code, the solution procedure is improved through the use of multigrid acceleration. For the viscous flows, the turbulence model of Spalart and Allmaras[16] is integrated to the wall without the use of wall functions. More details about the codes and the formulation can be obtained from Anderson and Bonhaus[13] and Anderson et al.[14]

Grid Generation Tools

The flow solutions are computed on unstructured grids. For two-dimensional applications, the code AFLR2[17,18] is used. It employs an advancing front method to generate high-quality grids for inviscid and viscous applications. In three dimensions, the code VGRIDns[19,20] is utilized to create the unstructured meshes. High aspect ratio cells are generated in the viscous regions with the advancing layers method.[19] In inviscid flow regions, the tetrahedral cells are constructed based on the advancing front algorithm.[20]

In the viscous flow region adjacent to a solid surface, the grid point distribution in the direction normal to the surface can be represented in general terms as[19]

$$\delta_i = \delta_1\left[1 + r_1(1 + r_2)^{i-1}\right]^{i-1} \tag{1}$$

This means that the normal grid spacing of the ith viscous layer δ_i is a function of the initial spacing at the wall δ_1 and the growth rates r_1 and r_2. The initial spacing δ_1 is chosen in order to have at least one grid point in the viscous sublayer. The growth rate r_1 is set to 0.15 and 0.40 for two- and three-dimensional calculations, respectively, and r_2 is zero. This choice for r_1 and r_2 is comparable to what is current practice in the field. With $r_1 = 0.5$ and $r_2 = 0.07$, the transonic, separated flow on the ONERA M6 wing has been computed accurately using a full viscous approach with a grid-resolved sublayer.[21]

Validation

Because we are interested in studying the flow around a strut–wall configuration, we will assess the accuracy of the flow solution with experimental data for a strut perpendicular to the walls of a wind tunnel.[22] The data are suitable only for in-tunnel CFD validation because the strut was enclosed by solid wind-tunnel walls above, below, and on the sides. The data were not corrected for the effect of blockage. The strut has a span $b = 340$ mm and a chord $c = 200$ mm. The walls above and below the model are located symmetrically at a distance of 300 mm away.

The strut was modeled with a span of 170 mm only, with a symmetry boundary condition applied to one of the side walls. The inflow plane is located 3000 mm upstream of the model to obtain a side wall boundary layer comparable to the one measured in the experiment. Downstream, the far-field boundary extends 2000 mm from the strut trailing edge. The first grid point is located 0.002 mm above the solid surfaces to provide at least one grid point within the viscous sublayer. The final grid contains 23, 082 surface nodes and a total of 367, 516 nodes.

The freestream Mach number is 0.73, and the Reynolds number is $Re_c = 6 \times 10^6$. The airfoil makes an angle of attack of 1.5 deg with respect to the incoming freestream velocity. A distance of 1050 mm upstream of the strut leading edge, the computed side wall boundary-layer displacement thickness δ^* and momentum thickness θ are equal to 2.75 and 2.16 mm, respectively. The predicted values of δ^* and θ are 16% lower than the experimental measurements. This can be explained by the grid spacing normal to the side walls being the same all of the way from the inflow plane to the outflow plane. There was no attempt to have finer normal grid spacing near the inflow plane where the boundary layer is much thinner than farther downstream. The growth of the boundary layer is, therefore, not captured precisely.

The calculated pressure distributions are compared to experimental measurements in Fig. 2. Note that the pressure distribution at $\eta = 0.6\%$ is located within the side wall boundary layer. For all locations, the agreement is good everywhere except on the upper surface by the shock generated near the midchord position. The predicted shock location is too far from the leading edge of the strut. For all cases, the pressure on the strut lower surface is almost in perfect agreement with the experimental data.

The normal force coefficient C_n computed at each span station along the wing is compared against the experimental data in Table 1. Because the flow solution did not predict the shock at the same location as in the experiment, that discrepancy causes the calculation to overestimate the experimental value of the normal force coefficient. However, the agreement is generally good. The experimental data show that the value of the normal force coefficient increases with the distance from the side wall. That trend is captured by the CFD solution as well. In light of these quite favorable results, we can be confident in applying the proposed tools to the modeling of flow near the junction of other similar configurations.

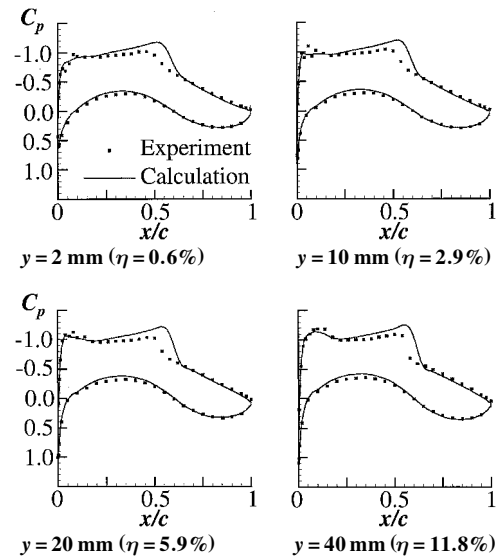

Fig. 2 C_p distribution for the AGARD test case: $M_\infty = 0.73$, $\alpha = 1.5$ deg, $Re_c = 6 \times 10^6$.

Table 1 Normal force coefficient C_n along the wingspan

Station y, mm (η, %)	Calculation	Experiment
$y = 2$ ($\eta = 0.6$)	0.6974	0.6651
$y = 10$ ($\eta = 2.9$)	0.7074	0.6830
$y = 20$ ($\eta = 5.9$)	0.7186	0.6885
$y = 40$ ($\eta = 11.8$)	0.7298	0.7127
$y = 80$ ($\eta = 23.5$)	0.7346	0.7186
$y = 170$ ($\eta = 50.0$)	0.7382	0.7205

Problem Description

The objective of this work is to perform a basic study of the interference drag of simple intersections in transonic flow. To simulate junctions found on airplanes, the case of the flow around a strut between parallel walls (Fig. 1) was analyzed for a cruise Mach number of $M_\infty = 0.85$ and an altitude of 40,000 ft. These yield a Reynolds number per meter of 5.3×10^6. For typical strut chords of 1 and 2 m, the corresponding Reynolds numbers are 5.3×10^6 and 10.6×10^6. The strut section makes an angle of attack $\alpha = 0$ deg with respect to the freestream flow for all of the calculations. To assess the effect of varying the thickness of the strut, symmetric airfoil sections of the NACA 64A family were studied with thicknesses t/c of 5 and 7.5%. Those airfoil sections are identified as NACA 64A005 and NACA 64A007.5. These dimensions are typical of the strut encountered in the course of the MDO studies[5,6] conducted on the strut-braced wing concept at Virginia Polytechnic Institute and State University. The scope of this study is, however, much broader and is not limited to that application.

As shown in Fig. 1, the strut is enclosed between two side walls, and the other faces of the computational box are open to the air. The domain extends 10 strut chords upstream, downstream, above, and below the strut to the far-field boundary. The distance chosen to the inflow and outflow planes is similar to what was used for the validation case presented in the preceding section. This choice is also based on the best judgment of the authors. Further analyses could consider variation of the thickness of the incoming side wall boundary layer. The parallel walls are five strut chords apart to achieve two-dimensional flow at midspan. The dihedral angle ϕ made by the strut with the adjacent wall was varied from 90 to 60 and 30 deg. No attempt was made at employing fairings or local shaping at the strut–wall intersection. The geometry is considered as a worst case from an airframer's point of view.

Calculation of the Interference Drag

The approach to determining the interference drag is to make use of the CFD tools as if one were performing an experiment in a wind tunnel. Solve the three-dimensional Navier–Stokes equations for the flow around a given strut–wall $(S + W)$ arrangement to determine $C_{L_{S+W}}$ and $C_{D_{S+W}}$, defined as

$$C_{L_{S+W}} = \frac{L_{S+W}}{q_\infty S_{\text{ref}}} \tag{2}$$

$$C_{D_{S+W}} = \frac{D_{S+W}}{q_\infty S_{\text{ref}}} \tag{3}$$

where the dynamic pressure is $q_\infty = (\gamma/2) p_\infty M_\infty^2$. The quantities $C_{L_{S+W}}$ and $C_{D_{S+W}}$ are obtained by integrating the pressure and skin friction over the strut surface only. The wall surface is not considered in the integration of the skin-friction force.

The reference area used to nondimensionalize the coefficients is determined in terms of the chord and the total length of the strut. Because the distance between the walls is set to five chords, it follows that

$$S_{\text{ref}} = 5c^2/\sin\phi \tag{4}$$

Hence, the definitions of the lift and drag coefficients become

$$C_{L_{S+W}} = (L_{S+W}/q_\infty)(\sin\phi/5c^2) \tag{5}$$

$$C_{D_{S+W}} = (D_{S+W}/q_\infty)(\sin\phi/5c^2) \tag{6}$$

A second Navier–Stokes analysis is performed to determine the lift and drag coefficients of the strut alone, without the effect of the walls, namely, C_{L_S} and C_{D_S}. Consider the strut–wall arrangement with $\phi = 90$ deg and apply the no-penetration, slip condition on the side walls, rather than the no-slip condition. The configuration is equivalent to a strut with symmetry planes at both ends. Hence, the strut is considered as having an infinite span in this case, just like when the analysis is performed on a two-dimensional airfoil. This yields

$$C_{D_S} = (D_S/q_\infty)(1/5c^2) \tag{7}$$

Twice the interference drag is calculated as the difference between the drag of the strut with the two walls and the drag of the strut without the effect of the walls. The result is nondimensionalized with respect to a conveniently chosen reference area to yield the interference drag coefficient $C_{D_{\text{interf}}}$. Early work by Hoerner[7] in the field of interference drag of struts suggests several possibilities for the choice of the reference area such as $S_{\text{ref}} = t^2$ or c^2, where t and c are the thickness and the chord of the strut, respectively. In this study, we opted for the latter expression.

Because the configuration contains two wall–strut intersections, we will have to take one-half of the drag difference:

$$D_{\text{interf}} = \tfrac{1}{2}(D_{S+W} - D_S) \tag{8}$$

The interference drag coefficient for one junction becomes

$$C_{D_{\text{interf}}} = \frac{D_{\text{interf}}}{q_\infty c^2} = \frac{1}{2}\left(\frac{D_{S+W} - D_S}{q_\infty c^2}\right) \tag{9}$$

Grid Convergence Study

The strut sections NACA 64A005 and 64A007.5 were obtained from the airfoil generation code LADSON.[23] For the inviscid calculations, the Euler equations were solved for each strut–wall angle ϕ on grids having a similar grid point distribution to ensure consistent results. Grid stretching along the length of the strut was used more extensively away from the wall. For the viscous calculations, the grids generated are based on a grid point distribution similar to the one used for the inviscid grids. For $Re_c = 5.3 \times 10^6$ and 10.6×10^6, a grid spacing at the wall $\delta_1 = 1 \times 10^{-5}$ per unit chord allows for at least one point in the sublayer of the turbulent boundary layer.

To assess the quality of the viscous grids generated for the NACA airfoil sections, a grid convergence study was performed for the NACA 64A007.5 section perpendicular to two viscous side walls. Only half the configuration was modeled with a symmetry plane at midspan. Three grids were generated, ranging from coarse to fine in terms of grid resolution. The overall grid characteristics are presented in Table 2. The triangulation of the plane of symmetry of the fine grid is shown in Fig. 3.

The Navier–Stokes flow solutions were obtained for the NACA airfoil sections for $M_\infty = 0.85$, $\alpha = 0$ deg, and $Re_c = 5.3 \times 10^6$. The pressure distributions are provided in Fig. 4 for several cross sections along the span of the strut. The major difference among these plots is the resolution of the shock at midchord. The finest grid provides the best result for resolving the shock. Another aspect worth mentioning, even if it is barely noticeable, is the presence of a sudden decrease in C_p right at the trailing edge of the strut for the coarse grid. This is because the grid is not refined enough at the trailing edge, thus leading to the formation of skewed cells there.

The magnitude of the lift coefficient is less than 6×10^{-4} for all grids. The drag coefficients are presented in Table 2. The pressure drag C_{D_p} varies quite significantly with grid refinement because of the poor shock resolution on the coarser grids. Despite that, the skin-friction drag C_{D_v} is almost constant for each case, resulting in

Table 2 Grid convergence for NACA 64A007.5: $\phi = 90$ deg, $M_\infty = 0.85$, $\alpha = 0$ deg, $Re_c = 5.3 \times 10^6$

Grid	Number of surface nodes	Total number of nodes	C_{D_p}	C_{D_v}	$C_{D_{\text{tot}}}$
Coarse	10,988	205,175	0.0059	0.0057	0.0116
Medium	15,321	299,862	0.0055	0.0057	0.0112
Fine	25,022	529,717	0.0052	0.0057	0.0110

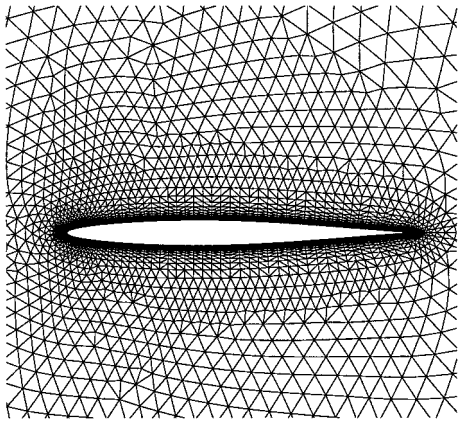

Fig. 3 Fine viscous grid at the plane of symmetry of the NACA 64A007.5 strut: $\phi = 90$ deg.

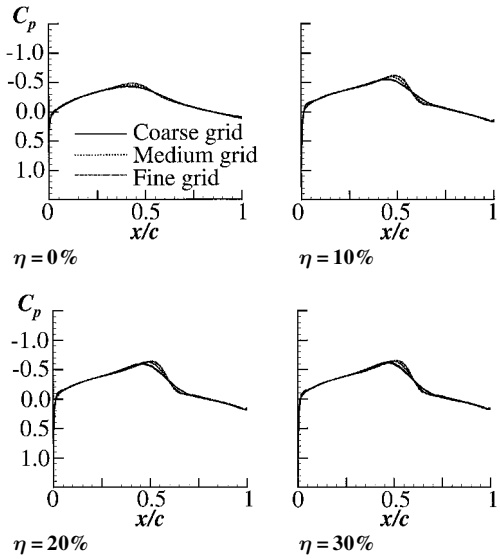

Fig. 4 Effects of grid refinement on C_p distribution for NACA 64A007.5 strut: $\phi = 90$ deg, $M_\infty = 0.85$, $\alpha = 0$ deg, $Re_c = 5.3 \times 10^6$ (Navier–Stokes solution).

an overall effect that depends mostly on the pressure drag. When the number of nodes is increased, the total drag coefficient seems to be reaching an asymptotic value. Therefore, the grid point distribution used for the fine mesh presented here was used throughout the viscous analyses shown later.

With the drag coefficients computed on the fine and medium grids in Table 2, an estimate of the discretization error on the drag coefficient can be calculated with Richardson extrapolation (see Ref. 24). The following development is based on the numerical flow solution being second-order accurate in space. Taking the grid refinement ratio r as the ratio of the number of nodes in the fine grid to the number of nodes in the medium grid, the exact value of the drag coefficient C_D is approximated by

$$C_{D_{\text{exact}}} \approx C_{D_{\text{fine}}} + \frac{C_{D_{\text{fine}}} - C_{D_{\text{medium}}}}{r^2 - 1} \tag{10}$$

To apply this method, the fine grid must be obtained by refining the medium grid equally in all directions. Unfortunately, this is not the case for the grids presented in Table 2 because, in the viscous layers, the grid point distribution normal to the surface is the same for all grids. Nevertheless, the approach is applied only to provide an estimate of the discretization error on the fine grid. It yields a value of $C_{D_{\text{exact}}} = 0.0108$, coresponding to an error of 0.0002 for the drag coefficient on the fine grid.

Another source of error is the criterion employed to determine the convergence of the CFD solution. For Euler and Navier–Stokes computations, the solution process was stopped after the drag coefficient reached an asymptotic value. This corresponds to a reduction of the residual by a factor of four orders of magnitude. It ensures that the results obtained for each arrangement are comparable with one another.

Results and Discussion

In this section, the results are presented for three-dimensional analyses performed on complete strut–wall configurations. Contour plots are used to highlight the most important features of the flow for the thicker strut in the region near the wall–strut junction. The effects of the relative strut thickness t/c, the strut–wall angle ϕ, and the Reynolds number Re_c on the interference drag are then evaluated from Euler and Navier–Stokes calculations.

Flowfield Details

Pressure contour plots and stream traces will be used to illustrate the behavior of the flow for the strut–wall configuration. Because the NACA 64A007.5 section exhibits the most interesting features in terms of separation and shock strength, the flow near the junction is presented for that case. Figure 5 depicts the Euler and Navier–Stokes solutions for the flowfield a distance 1×10^{-5} chord ($\eta = 0.0002\%$) from the side wall. The flow is from left to right, and the strut intersects the plane of the page coming down from above.

The Euler results are discussed first. For $\phi = 90$ deg, the symmetric strut section creates a symmetry in the pressure contours as well. The stagnation point is located at the leading edge of the strut. The fluid particles accelerate along the strut surface past the sonic conditions, accompanied by a decrease in the pressure. At $x/c = 0.60$, the pressure increases sharply as a consequence of the presence of a shock wave at that location. It then returns to its freestream value.

The $\phi = 60$ deg case shows the channel effect as the strut is tilted toward the side wall. The upper surface of the strut is located in that region. The stagnation point moves a short distance away from the leading edge on the upper surface. Also note that the pressure contours upstream of the strut leading edge extend farther away from it than for the $\phi = 90$ deg case. On the upper surface, the fluid is accelerated quickly as a result of the curvature of the strut surface and the proximity of the side wall. There is a large region of supersonic flow on the strut that culminates with a strong shock at $x/c = 0.75$. Overall, the presence of a tilted strut produces a lot of disturbance of the flowfield in the channel region. This is shown by the extent of the pressure contours above the strut. On the other hand, in the vicinity of the lower surface, the effect of the wall and the strut have a weaker effect in the flowfield than for $\phi = 90$ deg.

The configuration with $\phi = 30$ deg amplifies all of the trends already highlighted for $\phi = 60$ deg. The stagnation point moves

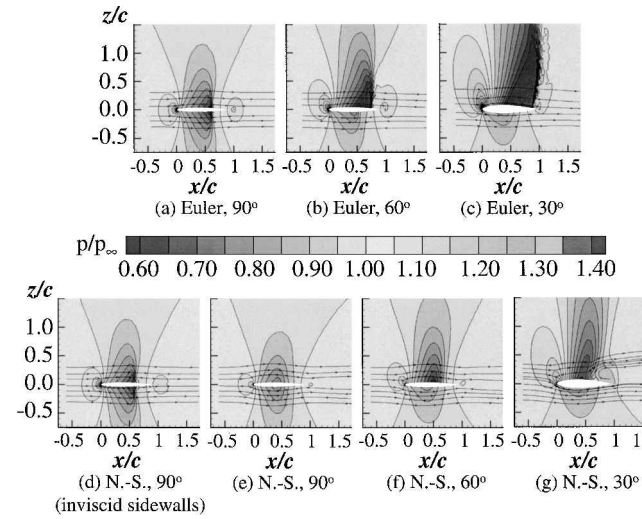

Fig. 5 Pressure contours with streamtraces at $\eta = 0.0002\%$ for the NACA 64A007.5 strut: $M_\infty = 0.85$, $\alpha = 0$ deg, $Re_c = 5.3 \times 10^6$. Euler solution: a) $\phi = 90$ deg, b) $\phi = 60$ deg, and c) $\phi = 30$ deg; and Navier–Stokes solution: d) $\phi = 90$ deg (inviscid side walls), e) $\phi = 90$ deg, f) $\phi = 60$ deg, and g) $\phi = 30$ deg.

downstream on the strut upper surface. The side wall is much closer to the strut upper surface, and, thus, the flow accelerates dramatically as depicted by the rapid variation in the pressure contours. The high-speed flow region ends at $x/c = 0.90$, where a very strong shock is formed. The flow goes from a very low pressure back to almost freestream condition over a very short distance. This produces a severe perturbation of the entire flowfield more than 1.5 chord above the strut. On the lower surface of the strut, the contours are considerably weaker than for $\phi = 90$ and 60 deg because the flow acceleration and deceleration back to freestream conditions are very smooth.

The Navier–Stokes results are shown for all angles, including the case where $\phi = 90$ deg with inviscid side walls. Because that case is two dimensional in nature, it allows a preliminary interpretation of the addition of viscous effects to the flow. The pressure contours are symmetric on both sides of the strut with the stagnation point located at the leading edge of the strut. The particles accelerate as they follow the strut surface until there is a sudden jump in pressure due to the presence of a shock at $x/c = 0.60$. The shock is smeared due to the viscous forces acting on the flow. It is weaker than the one obtained from the Euler calculation on the same configuration.

The contour plots for the cases remaining to be discussed all make use of the no-slip condition on the side walls as opposed to the case just presented. The cross sections are located within the side wall boundary layer. The $\phi = 90$ deg case exhibits symmetry in its pressure contours. As shown by the pressure contours confined to a small region upstream of the strut leading edge, the deceleration of the particles is small as they get to the stagnation point because they are within the side wall boundary layer. The variations in the flowfield are small because of the presence of the viscous side wall. This effect is beneficial because the shock displayed by the $\phi = 90$ deg case between inviscid side walls disappeared completely. The extent of the pressure contours in the flowfield is also made weaker by the viscous forces of the side wall boundary layer.

For $\phi = 60$ deg, the flow decelerates upstream of the strut and reaches the stagnation point a short distance from the leading edge along the upper surface. In the channel region, the particles' acceleration is accompanied by a drop in the pressure. Toward the trailing edge, the flow goes through a shock without separating. Compared to the Euler solution for the same configuration, the Navier–Stokes results show a shock made much weaker by the action of the viscous forces. The shock is located a significant distance upstream of the position predicted by the Euler solution, and it is also weaker. Additionally, because of the dissipative mechanism of the viscous forces, the pressure contours die out more quickly away from the strut. On the lower surface of the strut, the variations of the velocity are very small, and the absence of a shock there allows for a smooth pressure distribution. The boundary layers that develop on the strut and the adjacent side wall combine to deflect the fluid away from the low-speed flow regions adjacent to the strut surface.

The configuration for which $\phi = 30$ deg exhibits the most interesting features because of the much stronger interactions in the channel formed by the strut and the adjacent side wall. The fluid particles coming from upstream are deviated sharply away from the channel region due to the presence of the boundary layer. In the reduced space between the strut and the wall, the increase in the velocity of the fluid particles ends with a shock standing at $x/c = 0.60$. That smeared shock is weaker and upstream of the one predicted by the Euler solution due to the dissipative viscous effects. However, as a result of the severe adverse pressure gradient produced by the shock, the flow separates downstream. The stream traces show a large region of recirculating flow in the vicinity of the strut trailing edge. The fluid particles are deviated away from that vortex. The lower surface of the strut shows small variations in the pressure.

Pressure and Drag Coefficient Behavior

Euler Calculations

The pressure distributions along cross sections parallel to the walls are portrayed in Fig. 6 for the NACA 64A005 section and in Fig. 7 for the NACA 64A007.5 section. For the NACA 64A005 section, the flow is severely disrupted near the wall for $\phi = 60$ and 30 deg. The proximity of the side wall creates a channel that forces

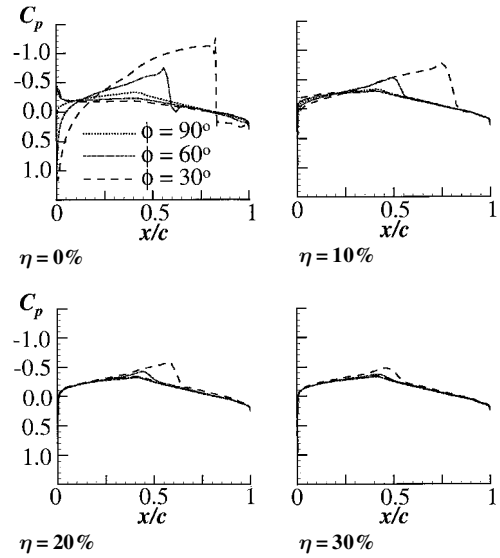

Fig. 6 C_p distribution for the NACA 64A005 strut, $M_\infty = 0.85$, $\alpha = 0$ deg (Euler solution).

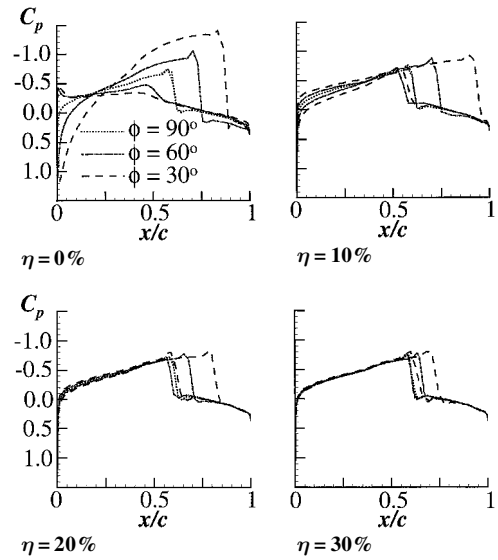

Fig. 7 C_p distribution for the NACA 64A007.5 strut, $M_\infty = 0.85$, $\alpha = 0$ deg (Euler solution).

the fluid to reach a higher velocity compared to the $\phi = 90$ deg case. Although the pressure distribution for $\phi = 90$ deg does not exhibit a shock, there is a strong shock for the $\phi = 60$ and 30 deg cases. The influence of the wall decays rapidly away from the wall. It is barely noticeable at $\eta = 30\%$ where the C_p curves almost fall on top of the $\phi = 90$ deg curves. For the NACA 64A007.5 section, the reduction of the strut–wall angle ϕ severely disrupts the flowfield in the region near the wall. The shocks for $\phi = 60$ and 30 deg are a lot stronger than for $\phi = 90$ deg. Shock effects are also felt a large distance away from the wall. Even at $\eta = 30\%$, the disturbance can be seen as the pressure distributions deviate significantly from the reference curve $\phi = 90$ deg.

The drag coefficients obtained for the Euler analyses are shown in Table 3. The magnitude of the lift coefficient is less than 3×10^{-4} for all cases. The results for $\phi = 90$ deg are in good agreement with equivalent two-dimensional airfoil computations performed at the same conditions on very fine grids. For the NACA 64A005 section, the drag is negligible for $\phi = 90$ deg because there is no shock along the strut surface. When the angle is reduced to $\phi = 60$ deg and then to $\phi = 30$ deg, the shock near the root observed in the pressure distribution in Fig. 6 becomes stronger and is responsible for the increase of the drag coefficient. For $\phi = 30$ deg, the shock persists over almost 20% of the strut span, although it is rendered much weaker as the

Table 3 Drag coefficients at $M_\infty = 0.85$

NACA airfoil	Intersection angle ϕ, deg	Euler $C_{D_{\text{tot}}}$	$Re_c = 5.3 \times 10^6$ C_{D_p}	C_{D_v}	$C_{D_{\text{tot}}}$	$Re_c = 10.6 \times 10^6$ C_{D_p}	C_{D_v}	$C_{D_{\text{tot}}}$
64A005	Two-dimensional airfoil	0.0001	0.0012	0.0060	0.0072	0.0011	0.0055	0.0066
	90 (inviscid side walls)	0.0002	0.0014	0.0058	0.0072	0.0013	0.0053	0.0066
	90	0.0002	0.0015	0.0059	0.0075	0.0014	0.0054	0.0069
	60	0.0004	0.0016	0.0060	0.0075	0.0016	0.0051	0.0067
	30	0.0039	0.0023	0.0060	0.0084	0.0023	0.0052	0.0075
64A007.5	Two-dimensional airfoil	0.0041	0.0056	0.0058	0.0114	0.0054	0.0053	0.0107
	90 (inviscid side walls)	0.0041	0.0058	0.0056	0.0114	0.0057	0.0051	0.0108
	90	0.0041	0.0052	0.0057	0.0110	0.0051	0.0052	0.0103
	60	0.0072	0.0069	0.0057	0.0126	0.0067	0.0049	0.0117
	30	0.0168	0.0110	0.0056	0.0166	0.0103	0.0049	0.0151

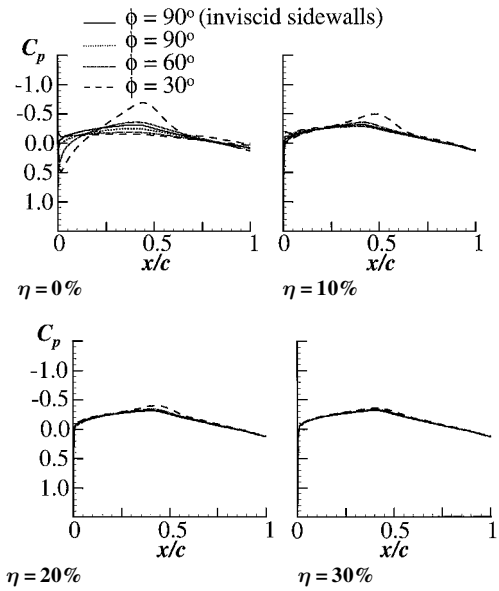

Fig. 8 C_p distribution for the NACA 64A005 strut: $M_\infty = 0.85$, $\alpha = 0$ deg, $Re_c = 5.3 \times 10^6$ (Navier–Stokes solution).

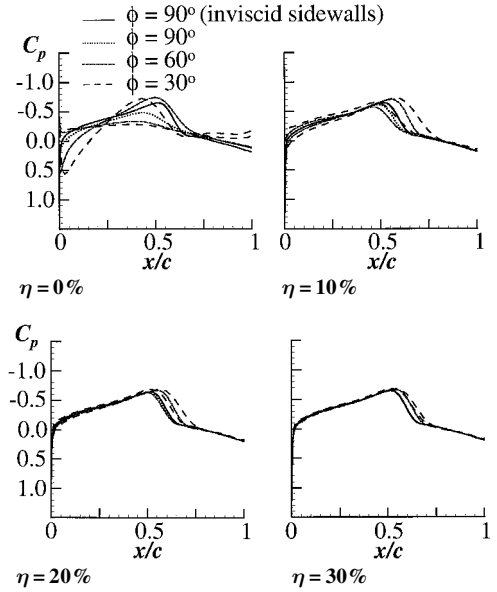

Fig. 9 C_p distribution for the NACA 64A007.5 strut: $M_\infty = 0.85$, $\alpha = 0$ deg, $Re_c = 5.3 \times 10^6$ (Navier–Stokes solution).

distance from the wall increases. For the NACA 64A007.5 strut section, the $\phi = 90$ deg arrangement has a large drag penalty because of the shock located at $x/c = 0.60$, as seen in Fig. 7. The reduction of the strut–wall angle to $\phi = 60$ and 30 deg is accompanied by an increase in the shock strength. The strength of the shock for $\phi = 30$ deg and its extent along the strut span explain the significant drag coefficient calculated for that case.

Navier–Stokes Calculations

Because there is little difference between the pressure plots at the two Reynolds numbers chosen for this study, only the pressure distributions for $Re_c = 5.3 \times 10^6$ are presented here. For the NACA 64A005 section results in Fig. 8, the viscosity dissipates the strong shock at the strut–wall junction very effectively, and the effect of the wall disappears very quickly as we move away from it. At a station $\eta = 30\%$, the perturbation in the pressure distributions is gone. This is accomplished more quickly than for the inviscid solution. The pressure distribution on the NACA 64A007.5 strut section is depicted in Fig. 9. As can be seen, there is a more dramatic influence of the wall in the vicinity of the junction. The flow separates at about $x/c = 0.65$ on the upper surface of the strut for the $\phi = 30$ deg case. However, from the other cross sections, we can see that the effect of the wall again dissipates rapidly as the distance along the span increases.

The lift coefficient is less than 0.005 in magnitude for all of the cases analyzed. The drag coefficients for $Re_c = 5.3 \times 10^6$ and 10.6×10^6 are listed in Table 3. For both strut thicknesses, two sets of results for $\phi = 90$ deg are presented, one involving viscous side walls (no-slip condition) and the other one representing the case for inviscid side walls (no-penetration, slip condition). The latter is used as a basis for comparing with an equivalent two-dimensional airfoil calculation done at the same conditions on a very fine grid. According to the results presented here, the calculation performed on a strut between parallel inviscid surfaces agrees well with its two-dimensional counterpart. The differences in the drag components tend to cancel out to yield a maximum discrepancy of about 0.0001 for the NACA 64A007.5 section at $Re_c = 10.6 \times 10^6$.

For the NACA 64A007.5 section at $\phi = 90$ deg, the presence of the viscous side walls alleviates the drag penalty obtained for the same strut between inviscid surfaces. On the other hand, the NACA 64A005 section does not exhibit favorable interference. In fact, the adjacent viscous walls cause the overall drag to increase by a few counts. For the NACA 64A005 strut section, the change of ϕ from 90 to 60 deg is accompanied by a negligible increase in drag because the strut section is still shockless. As opposed to the $\phi = 60$ deg case, the arrangement with $\phi = 30$ deg has a shock near the root, causing a net increase in the pressure drag. The drag coefficient for the NACA 64A007.5 strut shows a more rapid increase than the NACA 64A005 section as the strut–wall angle ϕ is reduced. When going from $\phi = 90$ to 60 deg, the pressure drag coefficient goes up due to the stronger shock. The increase in the drag coefficient for $\phi = 30$ deg can be explained by the strong shock and the large region of separated flow in the vicinity of the strut–wall junction. This is reflected in the pressure drag coefficient. Despite that, the pressure drag and even the overall drag coefficients are less than

Table 4 Interference drag coefficients

	$C_{D_{\text{interf}}} = D_{\text{interf}}/q_\infty c^2$		
ϕ, deg	Euler	$Re_c = 5.3 \times 10^6$	$Re_c = 10.6 \times 10^6$
	NACA airfoil 64A005		
90	0.0000	0.0006	0.0006
60	0.0007	0.0038	0.0028
30	0.0188	0.0238	0.0207
	NACA airfoil 64A007.5		
90	0.0000	−0.0010	−0.0011
60	0.0105	0.0080	0.0067
30	0.0739	0.0547	0.0487

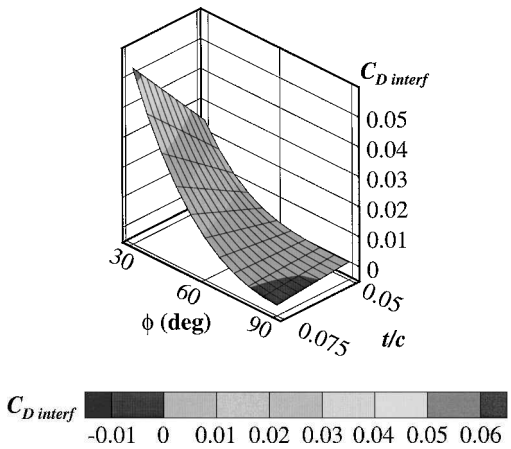

Fig. 10 Response surface with contours of $C_{D_{\text{interf}}}$ for $M_\infty = 0.85$, $\alpha = 0$ deg, $Re_c = 5.3 \times 10^6$.

the drag coefficient predicted by the Euler computations in Table 3. This confirms that the viscous effects can contribute favorably to the drag of the strut by alleviating the strength of the shock near the wall and by dissipating its effect rapidly in the flowfield.

All of the results presented in Table 3 can be interpreted in the form described by Eq. (9). For the Euler calculations, the case for which $\phi = 90$ deg was used as the reference C_{D_S}. For the Navier–Stokes analyses, the reference value for C_{D_S} is chosen as the value calculated for $\phi = 90$ deg between inviscid side walls. The results are listed in Table 4. The interference drag numbers highlight how dramatic the increase in drag is if the viscous effects are not considered. The NACA 64A007.5 airfoil with $\phi = 90$ deg exhibits favorable interference as the negative interference drag numbers suggest.

The statistical software JMP[25] was employed to fit a quadratic response surface to the interference drag coefficient using a standard least-squares procedure. Only the Navier–Stokes results were considered in this analysis. The equation can be included in design studies to account for the interference drag penalty of junctions. The response surface can be written as

$$C_{D_{\text{interf}}} = 0.1112 - 0.2572\sin\phi + 3.440(t/c) - 0.02097\log_{10} Re_c + 0.09009\sin^2\phi - 2.549(t/c)\sin\phi + 0.03010\log_{10} Re_c \sin\phi - 0.1462(t/c)\log_{10} Re_c \qquad (11)$$

where t/c is 0.05 for a 5%-thick airfoil. The response surface has a coefficient of determination $R^2 = 0.9987$ with an rms error of 0.001177. The curve is shown in Fig. 10 for $Re_c = 5.3 \times 10^6$.

Conclusions

In this work, unstructured grid methodology was applied to the Euler and Navier–Stokes equations to simulate the flow past strut–wall intersections and determine the interference drag of such junctions. The tools were validated against experimental data to assess the accuracy of the drag prediction. A strut enclosed by the walls of a wind tunnel was modeled, and the pressure distribution and side wall boundary-layer thickness were compared with experiment. There was good agreement of the calculated pressure distributions with the data.

The methodology was then applied to the study of a strut whose intersection angle with a flat wall was varied. The thickness and the Reynolds number were also changed to evaluate the effect of those parameters on the overall drag of the strut in the transonic flow regime. Both inviscid and viscous computations were conducted. Observations made based on the pressure distribution at several cross sections along the strut span showed the strong disturbance produced by the presence of the wall on the flowfield, causing the flow to separate in some instances. The viscous forces tended to alleviate the strength of the shocks induced near the junction of the strut with the wall. For the thicker strut perpendicular to the wall, the presence of the neighboring wall even created favorable interference. The disruption of the flowfield due to the influence of the side wall was stronger for the thicker strut section than for the thinner one. The strut–wall angle exhibited a strong correlation with the drag penalty as well. The effect of inclining the strut toward the wall increased the drag by a large factor compared to the case where the strut is perpendicular to the wall. A response surface for the interference drag coefficient was developed to take into account all of these effects and to help in the design of junctions.

Acknowledgments

This work was sponsored by NASA Langley Research Center, Grant NAG1-1852. Partial financial support for the first author was provided by Fonds pour la Formation de Chercheurs et l'Aide à la Recherche, Government of Quebec, Canada. The help provided by W. H. Mason is gratefully acknowledged. Special thanks also go to W. K. Anderson from NASA Langley Research Center for his invaluable help and suggestions, especially in the latest part of this project.

References

[1]Parikh, P., Pirzadeh, S., and Frink, N. T., "Unstructured Grid Solutions to a Wing/Pylon/Store Configuration," *Journal of Aircraft*, Vol. 31, No. 6, 1994, pp. 1291–1296.

[2]Agrawal, S., Creasman, S. F., and Lowrie, R. B., "Evaluation of Euler Solvers for Transonic Wing–Fuselage Geometries," *Journal of Aircraft*, Vol. 28, No. 12, 1991, pp. 885–891.

[3]Agrawal, S., Vatsa, V. N., and Kinard, T. A., "Transonic Navier–Stokes Flow Computations over Wing–Fuselage Geometries," *Journal of Aircraft*, Vol. 30, No. 5, 1993, pp. 791–793.

[4]Agarwal, R., "Computational Fluid Dynamics of Whole-Body Aircraft," *Annual Review of Fluid Mechanics*, Vol. 31, 1999, pp. 125–169.

[5]Gern, F. H., Gundlach, J. F., Ko, A., Naghshineh-pour, A. H., Sulaeman, E., Tétrault, P.-A., Grossman, B., Kapania, R. K., Mason, W. H., Schetz, J. A., and Haftka, R. T., "Multidisciplinary Design Optimization of a Transonic Commercial Transport with a Strut-Braced Wing," World Aviation Congress, WAC Paper 1999-01-5621, Oct. 1999.

[6]Gundlach, J. F., IV, Tétrault, P.-A., Gern, F. H., Naghshineh-Pour, A. H., Ko, A., Schetz, J. A., Mason, W. H., Kapania, R. K., Grossman, B., and Haftka, R. T., "Conceptual Design Studies of a Strut-Braced Wing Transonic Transport," *Journal of Aircraft*, Vol. 37, No. 6, 2000, pp. 976–983.

[7]Hoerner, S. F., "Interference Drag," *Fluid-Dynamic Drag: Practical Information on Aerodynamic Drag and Hydrodynamic Resistance*, Hoerner Fluid Dynamics, Midland Park, NJ, 1965, pp. 8-1–8-20.

[8]Kubendran, L. R., McMahon, H., and Hubbartt, J., "Interference Drag in a Simulated Wing–Fuselage Junction," NASA CR-3811, 1984.

[9]Barber, T. J., "An Investigation of Strut–Wall Intersection Losses," *Journal of Aircraft*, Vol. 15, No. 10, 1978, pp. 676–681.

[10]Roach, P. E., and Turner, J. T., "Secondary Loss Generation by Gas Turbine Support Struts," *International Journal of Heat and Fluid Flow*, Vol. 6, No. 2, 1985, pp. 79–88.

[11]Pierce, F. J., and Nath, S. K., "Interference Drag of a Turbulent Junction Vortex," *Journal of Fluids Engineering*, Vol. 112, No. 4, 1990, pp. 441–446.

[12]Tétrault, P.-A., "Numerical Prediction of the Interference Drag of a Streamlined Strut Intersecting a Surface in Transonic Flow," Ph.D. Dissertation, Dept. of Aerospace and Ocean Engineering, Virginia Polytechnic Inst. and State Univ., Blacksburg, VA, Jan. 2000, URL:http://etd.vt.edu/.

[13]Anderson, W. K., and Bonhaus, D. L., "An Implicit Upwind Algorithm for Computing Turbulent Flows on Unstructured Grids," *Computers and Fluids* Vol. 23, No. 1, 1994, pp. 1–21.

[14]Anderson, W. K., Rausch, R. D., and Bonhaus, D. L., "Implicit/Multigrid Algorithms for Incompressible Turbulent Flows on Unstructured Grids," *Journal of Computational Physics*, Vol. 128, 1996, pp. 391–408.

[15]Roe, P. L., "Approximate Riemann Solvers, Parameter Vectors and Difference Schemes," *Journal of Computational Physics*, Vol. 43, 1981, pp. 357–372.

[16]Spalart, P. R., and Allmaras, S. R., "A One-Equation Turbulence Model for Aerodynamic Flows," AIAA Paper 92-0439, Jan. 1992.

[17]Marcum, D. L., and Weatherill, N. P., "Unstructured Grid Generation Using Iterative Point Insertion and Local Reconnection," *AIAA Journal*, Vol. 33, No. 9, 1995, pp. 1619–1625.

[18]Marcum, D. L., "Generation of Unstructured Grids for Viscous Flow Applications," AIAA Paper 95-0212, 1995.

[19]Pirzadeh, S., "Three-Dimensional Unstructured Viscous Grids by the Advancing-Layers Method," *AIAA Journal*, Vol. 34, No. 1, 1996, pp. 43–49.

[20]Pirzadeh, S., "Structured Background Grids for Generation of Unstructured Grids by Advancing-Front Method," *AIAA Journal*, Vol. 31, No. 2, 1993, pp. 257–265.

[21]Frink, N. T., "Tetrahedral Unstructured Navier–Stokes Method for Turbulent Flows," *AIAA Journal*, Vol. 36, No. 11, 1998, pp. 1975–1982.

[22]Bartelheimer, W., Horstman, K. H., and Puffert-Meissner, W., "2-D Airfoil Tests Including Side Wall Boundary Layer Measurements," *A Selection of Experimental Test Cases for the Validation of CFD Codes*, Advisory Rept. 303, AGARD, 1994.

[23]Ladson, C. L., and Brooks, C. W., Jr., "Development of a Computer Program to Obtain Ordinates for NACA 6- and 6A- Series Airfoils," NASA TM X-3069, Sept. 1974.

[24]Roache, P. J., *Verification and Validation in Computational Science and Engineering*, Hermosa, Albuquerque, NM, 1998, Chap. 5, pp. 109–112.

[25]JMP Statistical Discovery Software, Ver. 3.1, SAS Inst., Inc., Cary, NC, 1995.

R. M. C. So
Associate Editor